Vision-and-Force-Based Compliance Control for a Posterior Segment Ophthalmic Surgical Robot

Ning Wang, *Graduate Student Member, IEEE*, Xiaodong Zhang, *Member, IEEE*, Danail Stoyanov, *Senior Member, IEEE*, Hongbing Zhang, and Agostino Stilli, *Member, IEEE*

***Abstract*—In ophthalmic surgery, particularly in procedures involving the posterior segment, clinicians face significant challenges in maintaining precise control of hand-held instruments without damaging the fundus tissue. Typical targets of this type of surgery are the internal limiting membrane (ILM) and the epiretinal membrane (ERM) which have an average thickness of only 60 μm and 2 μm, respectively, making it challenging, even for experienced clinicians utilising dedicated ophthalmic surgical robots, to peel these delicate membranes successfully without damaging the healthy tissue. Minimal intra-operative motion errors when driving both hand-held and robotic-assisted surgical tools may result in significant stress on the delicate tissue of the fundus, potentially causing irreversible damage to the eye. To address these issues, this work proposes an intra-operative vision-and-force-based compliance control method for a posterior segment ophthalmic surgical robot. This method aims to achieve compliance control of the surgical instrument in contact with the tissue to minimise the risk of tissue damage. In this work we demonstrate that we can achieve a maximum motion error for the end effector (EE) of our ophthalmic robot of just 8 μm, resulting in a 64% increase in motion accuracy compared to our previous work where the system was firstly introduced. The results of the proposed compliance control demonstrate consistent performance in the force range of 40 mN during membrane tearing.**

***Index Terms*—Ophthalmic surgery robot, compliance control, image-based measurement, force feedback.**

Manuscript received 6 April 2023; accepted 12 August 2023. Date of publication 7 September 2023; date of current version 18 September 2023. This letter was recommended for publication by Associate Editor J. Sheng and Editor J. P. Desai upon evaluation of the reviewers' comments. This work was supported in part by the Wellcome/EPSRC Centre for Interventional and Surgical Sciences (WEISS) under Grant 203145/Z/16/Z, in part by the Engineering and Physical Sciences Research Council (EPSRC) under Grants EP/P027938/1, EP/R004080/1, and EP/P012841/1, in part by the Royal Academy of Engineering Chair in Emerging Technologies Scheme under Grant CiET1819/2/36, and in part by the Science and Technology Project of Xi'an under Grant 21RGZN0007. For the purpose of open access, the authors have applied a CC BY public copyright licence to any author accepted manuscript version arising from this submission. *(Corresponding author: Agostino Stilli.)*

Ning Wang is with the School of Mechanical Engineering, Xi'an Jiaotong University, Xi'an 710049, China, and also with the Wellcome/EPSRC Centre for Interventional and Surgical Sciences, University College London, WC1E 6BT London, U.K. (e-mail: woseeing@163.com).

Xiaodong Zhang is with the School of Mechanical Engineering, Xi'an Jiaotong University, Xi'an 710049, China (e-mail: xdzhang@mail.xjtu.edu.cn).

Danail Stoyanov and Agostino Stilli are with the Wellcome/EPSRC Centre for Interventional and Surgical Sciences, University College London, WC1E 6BT London, U.K. (e-mail: danail.stoyanov@ucl.ac.uk; a.stilli@ucl.ac.uk).

Hongbing Zhang is with the No.1 Xi'an Hospital, Xi'an 710002, China (e-mail: zhanghongbing01@163.com).

This letter has supplementary downloadable material available at https://doi.org/10.1109/LRA.2023.3313065, provided by the authors.

Digital Object Identifier 10.1109/LRA.2023.3313065

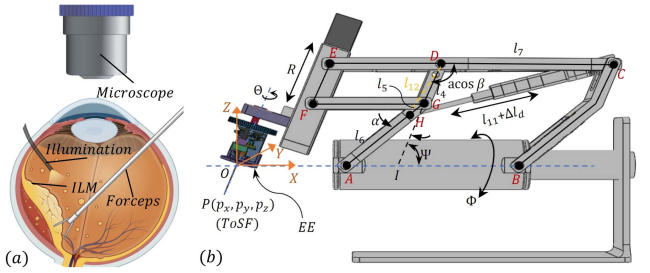

Fig. 1. Figure (a) presents an overview of the configuration of the surgical forceps, illumination source and microscope during ILM peeling. Figure (b) is the design of the OmSR system and its joint parameters. Please refer to our previous work [15], where the system has been introduced and its joint-link chain defined.

I. Introduction

ACCORDING to [1], approximately 2 billion individuals globally are affected by some forms of vision impairment, with nearly 200 million of them suffering from age-related macular degeneration. Retinal disorders are among the most common causes of permanent blindness in developed countries and, following cataracts, are the leading cause of blindness in developing countries. The challenges associated with fundus retina surgery are numerous, including the limited operating space (average eyeball diameter is 22 mm [2]), the inherent natural jitter of the arm of the clinician (magnitude is around 100 μm, frequency is about 10 Hz [3]), and the insufficient contact force between the surgical instrument and the fundus tissue to be accurately perceived by hand [4]. Due to these factors, the accuracy and the success rate of fundus surgery, particularly in ILM and ERM peeling surgery (see Fig. 1(a)), have yet to reach the desired level. Research shows that up to 50% of patients experience micro-injuries in the layer around the macula after peeling [5]. To overcome these limitations a number of robotic solutions have been explored [6] in the past few years. Although the handheld Micron system developed at Carnegie Mellon University [7] can reduce the natural jitter of the arm of the surgeon and provide feedback on the contact force during the operation, it increases the volume and mass of the tool, leading to lower ergonomics and a higher likelihood of fatigue. Furthermore, as shown in [7], its embedded auditory feedback exhibits a certain level of lag, which may lead to an inadequate level of protection for the fundus tissue. To address these limitations, the research community has focused on teleoperated solutions, such as the Preceyes Surgical system (Preceyes B.V., Eindhoven,

IEEE Robotics and Automation Letters (RA-L) paper, presented at ICRA 2024, Yokohama, Japan. Cite as RA-L paper.

NL), which was first used to evaluate the viability and safety of clinical intra-ocular robotic-assisted surgery at the University of Oxford [8]. Given the aim of reducing the uncertainty in surgeon judgement and automate repetitive surgical actions to minimise fatigue, the automated control of ophthalmic surgical robots has become a subject of intense research [9]. Both teleoperated control and automatic control methods have been developed, capable of meeting the requirements of following preset motion trajectories or the commands of a master controller [10]. However, mechanical errors resulting from structural processing and assembly and control errors arising from sensor measurement errors are inherent limitations in robot systems that cannot be fully mitigated. As highlighted in prior studies (e.g., [11]), even a small motion error in the surgical instrument at the EE can generate a significant force when the tool gets in contact with the fundus tissue, potentially causing local tissue deformation and damage. This is due to the structure of ophthalmic surgical robots that typically exhibits high structural stiffness to enhance movement accuracy while lacking the ability to adjust the EE position to compensate for sudden increases in contact force during surgical operations. Hardware-level improvements to meet the precision requirements of ophthalmic surgery are often expensive to achieve. As a result, research efforts have shifted toward improving motion accuracy through image-based guidance or force feedback compensation. For instance, Mach et al. [12] and the research group at Duke University [9] proposed a robot-assisted ophthalmic surgery method using Optical Coherence Tomography (OCT) for image-guided instrument control. This approach enhances motion accuracy compared to open-loop control but is challenged by the large noise interference and slow image processing speed of OCT images. He et al. from Johns Hopkins University [13] introduced an active interventional control framework based on contact force to predict excessive-force instances and avoid tissue damage by providing reminders to the surgeon. Li et al. [11] proposed an admittance-controlled amplified force tracking scheme for lumbar puncture surgical robots, enabling a desirable interaction force profile to be perceived by the operator. Admittance control [14] is a real-time, effective method for active compliance control that does not require sophisticated model-based control strategies. Nevertheless, the assumption underlying these methods is that the motion of the surgical robot is perfectly accurate and without any motion error. In the presence of motion errors, the contact force used to adjust the instrument position would result in superimposed errors, compromising the ability to reach the desired position.

In this work a vision-and-force-based compliance control method that relies on admittance control for a posterior segment surgical system is proposed. The method aims at emulating the sensory information perceived by surgeons during surgery to achieve high precision and safe tool-tissue interaction in fundus surgery. The main contributions of this work is a double-loop admittance controller which enables the dynamical adjustment of the Tip of the Surgical Forceps (ToSF) based on the magnitude of the contact force between the ToSF and the fundus tissue, achieving variable stiffness compliance control; this also embeds a nested position control loop to provide position feedback and compensate for the movement errors of the EE of the Ophthalmic micro-Surgery Robot (OmSR) during clinical surgery. To overcome the lack of proximity sensors that can be integrated on the EE of such a small tool, the position measurement is purely based on visual feedback. We address the problem of estimation of the relative position between the microscope coordinate system and the robot coordinate system at software level using the Efficient-Perspective-n-Point (EPnP), feature matching, and error optimisation methods based on Lie group algebra. The OmSR is shown in Fig. 1(b).

This work is structured as follows: in Section II, the proposed admittance control is presented, followed by a discussion on interaction force measurement and the relative positional relationship between the microscope and the OmSR. The motion compensation error of the ToSF based on visual depth estimation is also explained. In Section III, the setup of the OmSR is described, along with the experimental results and performance of the proposed method. Finally, the conclusions of this work are presented in Section IV.

II. Vision-and-Force-Based Compliance Control

A. Admittance Control Mathematical Method

The proposed admittance control method implements a virtual mass-spring-damper model of the EE and the OmSR joint to regulate the contact force between the ToSF and the fundus tissue ensuring that the damage threshold for the tissue is not exceeded by adjusting accordingly the position of the ToSF. As detailed in the next section, the proposed model is benchmarked using the force feedback from a force sensor installed underneath the target phantom. While this is obviously not a clinically realistic scenario, it is a useful approach to evaluate the performance of the proposed controller. Clinical integration will be enabled by embedded sensors in future iterations of the OmSR system. A transfer function between the expected and the measured contact forces and the position adjustments of the ToSF is defined. The proposed control method adjusts the position of the ToSF based on the changes in the magnitude of the interaction force, enabling compliance control. As highlighted in Section I, relying solely on the contact force as the input of the OmSR could result in the superimposition of motion errors of the ToSF onto the admittance control method and pose potential safety hazards due to sensor inaccuracy or excessive transient noise. To compensate for these errors and improve movement accuracy and surgical safety, the proposed admittance control also utilises the real-time position of the ToSF, as measured by the microscope, as input for motion error compensation.

The OmSR can be modelled as following:

$$F - F_d = \mathbf{M}_d \left(\ddot{\mathbf{P}} - \ddot{\mathbf{P}}_d \right) + \mathbf{B}_d \left(\dot{\mathbf{P}} - \dot{\mathbf{P}}_d \right) + \mathbf{K}_d \left(\mathbf{P} - \mathbf{P}_d \right) \tag{1}$$

Based on this model we can define the proposed admittance controller as detailed in the next paragraphs. Please refer to Fig. 2 where the control scheme is presented. Here F and F_d represent the sensor-measured and desired contact forces between the fundus lesion and the ToSF respectively. The model of the system includes the inertia matrix ($\mathbf{M}_d$), the damping matrix ($\mathbf{B}_d$), and

IEEE Robotics and Automation Letters (RA-L) paper, presented at ICRA 2024, Yokohama, Japan. Cite as RA-L paper.

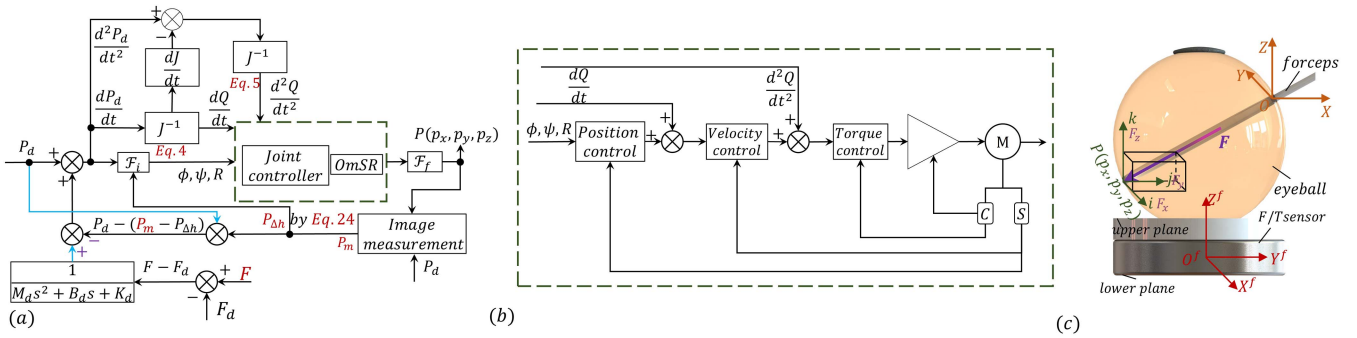

Fig. 2. Proposed admittance control scheme is depicted in figure (a). $\mathcal{F}_f$ and $\mathcal{F}_i$ represent the forward and inverse kinematics of the OmSR, respectively. $\mathbf{P}_m$ is the position measured by microscope. When $0 < \mathbf{F} \leq \mathbf{F}_d$, the control loop involving the interaction force is activated, as shown by the blue line. The internal sub-module framework of every joint position controller module is presented in figure (b). The joint drive motors are represented by $\mathbf{M}$, and the *S* and *C* represent encoders and electric current, respectively. Figure (c) depicts the F/T sensor phantom integration to measure the contact force between the ToSF and the fundus tissue. The purple arrow represents the contact force $\mathbf{F}$, which is decomposed in $\mathbf{F}_x$, $\mathbf{F}_y$, along $\mathbf{F}_z$ on the $\boldsymbol{i}$, $\boldsymbol{j}$, $\boldsymbol{k}$ axes, which are parallel to X^f, Y^f, and Z^f axes of the F/T sensor coordinate system $O^f X^f Y^f Z^f$.

the stiffness matrix ($\mathbf{K}_d$). $\ddot{\mathbf{P}}$, $\dot{\mathbf{P}}$, and $\mathbf{P}$ are the acceleration, velocity, and position defining the real trajectory of the ToSF, while $\ddot{\mathbf{P}}_d$, $\dot{\mathbf{P}}_d$, and $\mathbf{P}_d$ represent the desired acceleration, velocity, and position of the ToSF, respectively. The deviation between F and F_d is represented by $\Delta F = F - F_d$, and the deviation between $\mathbf{P}$ and $\mathbf{P}_d$ of the ToSF is represented by $\Delta\mathbf{P} = \mathbf{P} - \mathbf{P}_d$. Thus, the desired acceleration of the ToSF can be calculated as:

$$\ddot{\mathbf{P}}_d = \ddot{\mathbf{P}} + {\mathbf{M}_d}^{-1}(\mathbf{B}_d \cdot \Delta\dot{\mathbf{P}} + \mathbf{K}_d \cdot \Delta\mathbf{P} - \Delta F) \tag{2}$$

In order to better express the actual physical meaning of $\ddot{\mathbf{P}}$, $\dot{\mathbf{P}}$ in OmSR, the differential forms of them ($\frac{d\mathbf{P}}{dt}$, $\frac{d^2\mathbf{P}}{dt^2}$) will be used for derivation and interpretation in the following sections. The Cartesian position of ToSF directly depends on the configuration of the joints, in specific as shown in Fig. 1(b), on the Degrees of Freedoms (DOFs) Ψ, Φ, R, Θ and γ according to the forward kinematics of OmSR we proposed in [15].

$$\mathbf{P} = \mathcal{F}_f(\mathbf{Q}) = R \begin{bmatrix} -\cos\Psi \\ \sin\Phi \\ -\sin\Psi\cos\Phi \end{bmatrix} \tag{3}$$

$\mathbf{Q} = [\Psi, \Phi, R, \Theta, \gamma]^T$ are the joint coordinates of the OmSR system. Φ, Ψ and Θ represent the rotational DOFs around the X-axis, Y-axis, and the axis of rotation of the forceps respectively, while R represents the translational DOF along the rod EF. γ represents the opening and closing DOF of the forceps.

Given the small size of the forceps and the low speed imposed to them during the opening and closing process, it is assumed that their motion will not significantly affect the velocity of the ToSF. Thus, the first and second derivatives of Θ and γ with respect to time are considered to be zero. As a result, the desired velocity $\frac{d\mathbf{P}}{dt}$ and desired acceleration $\frac{d^2\mathbf{P}}{dt^2}$ of the ToSF are only dependent on Ψ, Φ, and R. Thus, these quantities can be expressed as:

$$\frac{d\mathbf{P}_d}{dt} = \boldsymbol{J} \cdot \frac{d\mathbf{Q}}{dt}, \quad \frac{d^2\mathbf{P}_d}{dt^2} = \frac{d\boldsymbol{J}}{dt} \cdot \frac{d\mathbf{Q}}{dt} + \boldsymbol{J} \cdot \frac{d^2\mathbf{Q}}{dt^2} \tag{4}$$

Where $d\mathbf{Q}/dt$ is the velocity of OmSR joints, and $d\mathbf{Q}/dt = [d\Psi/dt, d\Phi/dt, dR/dt]^T$. $d^2\mathbf{Q}/dt^2$ is the acceleration of the OmSR joints, $d^2\mathbf{Q}/dt^2 = [d^2\Psi/dt^2, d^2\Phi/dt^2, d^2R/dt^2]^T$. $\boldsymbol{J}$ is the Jacobian matrix (see in (6)) of the OmSR, which describes the relationship between the movement of the ToSF in the Cartesian space and the joint space of the robot. Consequently, the acceleration of the OmSR joints can be determined as follows:

$$\frac{d^2\mathbf{Q}}{dt^2} = \boldsymbol{J}^{-1}\left(\frac{d^2\mathbf{P_d}}{dt^2} - \frac{d\boldsymbol{J}}{dt} \cdot \frac{d\mathbf{Q}}{dt}\right) \tag{5}$$

$$\boldsymbol{J} = \begin{bmatrix} dp_x/d\Psi & dp_x/d\Phi & dp_x/dR \\ dp_y/d\Psi & dp_y/d\Phi & dp_y/dR \\ dp_z/d\Psi & dp_z/d\Phi & dp_z/dR \end{bmatrix} \tag{6}$$

The rotational DOF, Ψ, is driven by the linear push rod motor installed between the AD linkage and the BC rod. Hence, the change in Ψ is represented by the elongation, Δl_d, of the linear motor. The relationship between Ψ and Δl_d can be established by considering the length of the links of our system and their positional relationship, as shown in Fig. 1(b).

$$\Psi = \operatorname{asin}\frac{l_5\sin\alpha}{l_{12}} + \pi - \operatorname{acos}\frac{l_{12}^2 + l_7^2 - (\Delta l_d + l_{11})^2}{2l_7 l_{12}} \tag{7}$$

Where $l_{12} = \sqrt{l_4^2 + 2l_4 l_5\cos\alpha + l_5^2}$.

Let $\beta = (l_{12}^2 + l_7^2 - (\Delta l_d + l_{11})^2)/(2l_7 l_{12})$. The $dp_x/d\Psi$ and $dp_z/d\Psi$ represented by Δl_d and other elements in $\boldsymbol{J}$ can be shown as:

$$\frac{dp_x}{d\Psi} = -\frac{2R\,(\Delta l_d + l_{11})\sin\left(\operatorname{acos}\beta - \operatorname{asin}\frac{l_5\sin\alpha}{l_{12}}\right)}{l_7 l_{12}\sqrt{4-\beta^2}} \tag{8}$$

$$\frac{dp_y}{d\Psi} = 0 \tag{9}$$

$$\frac{dp_z}{d\Psi} = -\frac{2R\,(\Delta l_d + l_{11})\cos\left(\operatorname{acos}\beta - \operatorname{asin}\frac{l_5\sin\alpha}{l_{12}}\right)}{l_7 l_{12}\sqrt{4-\beta^2}} \tag{10}$$

$$\frac{dp_x}{d\Phi} = 0, \frac{dp_y}{d\Phi} = R\cos\Phi, \frac{dp_z}{d\Phi} = R\sin\Psi\sin\Phi \tag{11}$$

$$\frac{dp_x}{dR} = -\cos\Psi, \frac{dp_y}{dR} = \sin\Phi, \frac{dp_z}{dR} = -\sin\Psi\cos\phi \tag{12}$$

The Jacobian matrix $\boldsymbol{J}$ and the inverse of the Jacobian matrix $\boldsymbol{J}^{-1}$ can be expressed using the above formulas from (8) to (12).

The differentiation of the Jacobian matrix with respect to time ($\frac{d\boldsymbol{J}}{dt}$) can be expressed as:

$$\frac{d\boldsymbol{J}}{dt} = \frac{d\mathbf{P}_d}{d\mathbf{Q} \cdot dt} \tag{13}$$

Therefore, by means of sequential derivation of these formulas, the complete expression of the functional relationship between the motion parameters of the ToSF and of the OmSR joints can be calculated using (2). Furthermore, the implementation of compliance control for the OmSR can be achieved.

B. Double-Loop Admittance Controller

The proposed admittance control scheme is depicted in Fig. 2(a). When no forces are detected by the sensor, the ToSF is driven by the joint position controllers purely based on the real-time image-based position feedback. In this case the force control loop is not activated. If a force is detected and its magnitude is less than the maximum desired contact force, the ToSF is controlled to the desired position while maintaining the interaction force under the maximum desired force threshold through a combination of force position control and position feedback (as illustrated by the blue line in Fig. 2(a)). The admittance controller continuously calculates and adjusts the desired velocity and acceleration and inputs these parameters into the joint controllers of each joint. The joint controllers of the OmSR use a PID control mode and comprise three sub-control modules: position control, speed control, and torque control. Position feedback for each joint is obtained from a sensor/encoder installed on the output shaft of each motor and the first-order and second-order derivatives are calculated and fed back to the speed control module and torque control module, respectively.

C. Interaction Force Measurement

The measurement of the contact force between the ToSF and fundus tissue in the clinical application of this system will be facilitated by a three-dimensional force sensor based on Fiber Bragg Gratings (FBGs) as the one presented in [16]. Research from this group on the optimisation of the parameters of the FBG-based force sensor for this application is still ongoing. A dedicated publication on this research topic is currently under preparation. Nonetheless, the focus of this work is not on the design and performance optimisation of the FBG sensor as its main role is to serve as an input for the admittance control method, to enable compliant control of OmSR; instead we focus on the control method regardless of how the force is measured. In light of this, a state-of-art industrial Six-axis Force/Torque (F/T) Sensor mini40 (ATI Industrial Automation, Inc., Apex, NC, US) with high signal-to-noise ratio and resolution is utilised to measure the contact force indirectly by pairing it with the targeted phantom eye used in the experiments described in the following sections. Doing so we can overcome the challenges associated with the lack of space to apply the F/T sensor on the EE as well as its load limitations. Specifically, the base of the F/T Sensor is fixed on the experimental platform and the eyeball phantom is placed on the top sensing surface, allowing for indirect measurement of the contact force values. The relative positioning between the eyeball and the sensor is depicted in Fig. 2(c). It is worth noticing that the sensitivity of the FBGs force sensor used in [17] i.e. 0.35 mN is higher than the one of the F/T sensor used in our test rig.

The F/T Sensor is capable of measuring forces and torques in the three Cartesian coordinates, allowing for measurement of the contact force components - F_x, F_y, F_z along the $\boldsymbol{i}$-axis, $\boldsymbol{j}$-axis, $\boldsymbol{k}$-axis. The magnitude of the contact force $\mathbf{F}$ can be calculated as:

$$F = \sqrt{F_x^2 + F_x^2 + F_y^2} \tag{14}$$

Where F is the module of the force $\mathbf{F}$.

D. Relative Position Between Microscope and OmSR

As stated in Section.II-C, the highly integrated nature of the EE installed on the OmSR, with a diameter of 0.5 mm for the 25 Gauge intra-ocular surgical forceps and the small volume of the eyeball, typically less than 6 cm^3, precludes the installation of a proximity sensor on the EE to measure the position of the ToSF and give the position feedback for the admittance control loop in clinical surgery. To overcome this challenge, in this work we propose a microscope image-based measurement method to accurately estimate the position of the ToSF in the Cartesian space. The coordinate of the ToSF in the pixel coordinate system is obtained through target recognition and image processing techniques. Subsequently, the (15) is used to transform the coordinate of the ToSF from the pixel coordinate system to the Cartesian coordinate system of the OmSR, thus facilitating the measurement of the depth of ToSF with respect to the reference frame of the microscope. It is important to note that the microscope images being monocular, lack depth information. Even in advanced commercial digital systems the user can only get a rough estimation of the depth of surgical tools in the field of view of the microscope [18]. As usual in robotic applications, the vectorial position of point $\mathbf{P} = [p_x, p_y, p_z]^T$ of the ToSF in the Cartesian space is expressed as a homogeneous vector $\mathbf{P}_{hc} = [p_x, p_y, p_z, 1]^T$ and the pixel coordinates of $\mathbf{P}$ is rewritten as $\boldsymbol{u} = [u, v, 1]^T$. The relationship between $\mathbf{P}_{hc}$ and $\boldsymbol{u}$ can be expressed as follows:

$$h \begin{bmatrix} u \\ v \\ 1 \end{bmatrix} = \boldsymbol{K} \exp(\xi^{\wedge}) \begin{bmatrix} p_x \\ p_y \\ p_z \\ 1 \end{bmatrix} \tag{15}$$

Where $\boldsymbol{K}$ is the microscope intrinsic transformation matrix, which can be obtained from the microscope datasheet. h is the image depth between point $\mathbf{P}$ and the microscope. ξ, a six-dimensional vector, is the element of the Lie algebra $\mathfrak{se}(3)$ [19] which can be expressed as:

$$\mathfrak{se}(3) = \left\{ \xi = [\rho, \phi]^T \in \mathbb{R}^6, \phi \in \mathfrak{so}(3), \exp(\xi^{\wedge}) \right\} \tag{16}$$

$\rho \in \mathbb{R}^3$ is the three-dimensional translation vector. ϕ is the element of the Lie algebra $\mathfrak{so}(3)$. $\wedge$ is the skew-symmetric matrix and converts a 6-dimensional vector into a 4-dimensional vector. $\exp()$ is called the exponential map in Lie groups and

IEEE Robotics and Automation Letters (RA-L) paper, presented at ICRA 2024, Yokohama, Japan. Cite as RA-L paper.

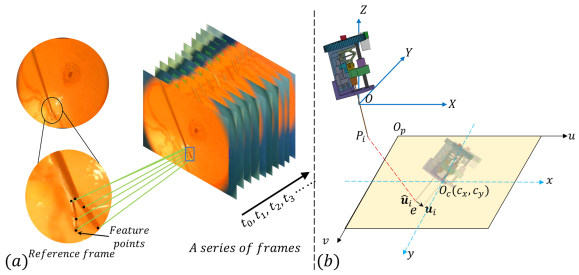

Fig. 3. Figure (a) displays a schematic representation of the process used to obtain the pixel coordinates of the ToSF via image processing. The rectangular box, shown in blue in the target image, is generated by the CSR-DCF algorithm, and the green line represents the connection of feature points matched using the SIFT method. In figure (b), the $\boldsymbol{e}$ is the pixel error. The pixel coordinate system is represented by O_puv, while the microscope coordinate system is represented by O_cxy, with the $\boldsymbol{u}$ axis being parallel to the $\boldsymbol{x}$ axis and the $\boldsymbol{v}$ axis being parallel to the $\boldsymbol{y}$ axis.

Lie algebras. $\exp(\xi^\wedge) = \begin{bmatrix} \boldsymbol{R} & t \\ \boldsymbol{0}^T & 1 \end{bmatrix} \in \mathbb{R}^{4\times4}$, which represents the extrinsic transformation matrix. $\boldsymbol{R} \in \mathbb{R}^{3\times3}$ and $t \in \mathbb{R}^3$ are the rotation and translation matrix of the microscope in OmSR coordinate system, respectively.

In clinical settings we envision the OmSR to be installed on the side of the headrest in the operating room (OR) and positioned near the head of the patient prior to the surgical procedure. To obtain clear intra-operative imaging the objective lens of the microscope is adjusted before the operation. As a result, the relative position of the microscope and the OmSR in the OR is not fixed, making it difficult to manually measure their relative position with high precision. Hence, in this letter, we employ the EPnP method [20] to estimate the extrinsic transformation matrix $\exp(\xi^\wedge)$ between the microscope and OmSR at software level, thus obtaining the rotation ($\boldsymbol{R}$) and translation matrix ($\mathbf{t}$).

We estimate $\exp(\xi^\wedge)$ by using the coordinates of n non-coplanar points of ToSF in Cartesian space and the corresponding pixel coordinates of n points in the pixel coordinate system, as described in (15) based on EPnP method. To perform this task, the forward and inverse kinematics of OmSR are calculated, enabling the controller of the OmSR to accurately output the Cartesian coordinates of the ToSF. At the same time, the pixel coordinates of ToSF in the field of view of the microscope can be obtained through feature processing methods. As shown in Fig. 3(a), a set of feature points is generated by extracting the features of the ToSF from a reference frame, using the Scale Invariant Feature Transform (SIFT) method proposed in [21]. The Channel and Spatial Reliability of the Discriminative Correlation Filter (CSR-DCF) algorithm [22] is then used to identify and track the position of ToSF in the target image, framing it within a rectangular box. The same SIFT method is applied to the region framed by the rectangular box in the target image to extract all the feature points. The pixel coordinates of the ToSF in the target image can be obtained by performing feature point matching and correction on the set of feature points extracted from the rectangular box and the reference frame. Here, all the frames in the time series considered, including the reference one, are acquired by the clinical microscope. The reference frame contains all the characteristic features of the ToSF, e.g. the tips of the two flips and the centre of rotation of flips, and it works as a reference template to extract such features in the frame acquired at time ($\boldsymbol{t_i}$).

As depicted in Fig. 3(b), an error $\boldsymbol{e}$ between the theoretical pixel coordinate $\hat{\boldsymbol{u}}_i$ and the actual pixel matched to it in the coordinate $\boldsymbol{u}_i$ will be typically present, due to the occurrence of noise in the feature matching and in the ToSF tracking processes. To determine the optimal $\exp(\xi^\wedge)$, a least squares problem is devised to minimise the sum of errors associated with the pixel coordinates of n non-coplanar points, as expressed by:

$$\xi^* = arg\ \min \frac{1}{2} \sum_i^n \left\| \boldsymbol{u}_i - \frac{1}{h_i} \boldsymbol{K} \exp(\xi^\wedge) \mathbf{P}_i \right\|_2^2 \tag{17}$$

Where $\mathbf{P}_i$, h_i and $\boldsymbol{u}_i$ represents the $i-th$ point $\mathbf{P}$ in Cartesian space, the depth of $i-th$ point $\mathbf{P}$ and the pixel coordinate of $i-th$ point $\mathbf{P}$ respectively.

For the optimisation of the total errors ξ^*, it is necessary to consider the relationships between multiple pairs of $\mathbf{P}$ and $\boldsymbol{u}$. This leads to the construction of a least squares problem as a Lie algebra unconstrained optimisation problem [23]. The derivative of the matching error $\boldsymbol{e}$ with respect to the optimisation variable ξ is then computed, and the solution is obtained through the Levenberg-Marquardt (LM) optimisation algorithm [24]. The computational process for the derivative can be linearised as:

$$\boldsymbol{e}(\xi + \delta\xi) \approx \boldsymbol{e}(\xi) + \boldsymbol{J}_c \cdot \delta\xi \tag{18}$$

Where $\boldsymbol{e}$ is the pixel coordinate error. $\boldsymbol{J}_c \in \mathbb{R}^{2\times6}$ is Jacobian matrix.

The derivative of Lie algebra in the above (18) can be solved by the perturbation model [25]. ξ is left multiplied by perturbation quantity $\delta\xi$. The derivative of $\boldsymbol{e}$ with respect to the perturbation quantity $\delta\xi$ can be expressed as:

$$\frac{\partial \boldsymbol{e}}{\partial \delta\xi} = \lim_{\delta\xi\to0} \frac{\boldsymbol{e}(\delta\xi \oplus \xi)}{\delta\xi} = \frac{\partial \boldsymbol{e}}{\partial \mathbf{P}^c} \frac{\partial \mathbf{P}^c}{\partial \delta\xi} \tag{19}$$

Where $\oplus$ represents the left multiplication associated with the perturbation in the Lie algebra. $\mathbf{P}^c = (\exp(\xi^\wedge)\mathbf{P})_{1:3} = [x^c, y^c, Z^c]^T$ is the coordinate of the point $\mathbf{P}$ in the microscope coordinate system. $1:3$ extracts the first three dimension values. The microscope camera model can be expressed as:

$$h \begin{bmatrix} u \\ v \\ 1 \end{bmatrix} = \begin{bmatrix} f_x & 0 & c_x \\ 0 & f_y & c_y \\ 0 & 0 & 1 \end{bmatrix} \begin{bmatrix} x^c \\ y^c \\ z^c \end{bmatrix} \tag{20}$$

Here f_x and f_y are the differentials of microscope focal length f on the x-axis and y-axis respectively. $[c_x, c_y]$ is the pixel coordinate of the origin O_c of the microscope coordinate system O_cxy.

Thus, $\frac{\partial \boldsymbol{e}}{\partial \mathbf{P}^c}$ and $\frac{\partial \mathbf{P}^c}{\partial \delta\xi}$ are specifically expressed as:

$$\frac{\partial \boldsymbol{e}}{\partial \mathbf{P}^c} = -\begin{bmatrix} \frac{f_x}{z^c} & 0 & -\frac{f_x x^c}{z^{c2}} \\ 0 & \frac{f_y}{z^c} & -\frac{f_y y^c}{z^{c2}} \end{bmatrix}, \frac{\partial \mathbf{P}^c}{\partial \delta\xi} = \frac{\partial \exp(\xi^\wedge)\mathbf{P}}{\partial \delta\xi}_{1:3} \tag{21}$$

The $\boldsymbol{J}^c$ in (17) is equal to $\dfrac{\partial \boldsymbol{e}}{\partial \delta \xi}$ which can be expressed as:

$$\begin{bmatrix} \frac{f_x}{z^c} & 0 & -\frac{f_x x^c}{z^{c2}} & -\frac{f_x x^c y^c}{z^{c2}} & f_x + \frac{f_x x^2}{z^{c2}} & -\frac{f_x y^c}{z^c} \\ 0 & \frac{f_y}{z^c} & -\frac{f_y y^c}{z^{c2}} & -f_y - \frac{f_y y^{c2}}{z^{c2}} & \frac{f_y x^c y^c}{z^{c2}} & \frac{f_y x^c}{z^c} \end{bmatrix} \tag{22}$$

The Jacobian matrix $\boldsymbol{J}^c$ represents the first-order derivative of the error $\boldsymbol{e}$ with respect to the Lie algebra of the relative position between the microscope and the OmSR. The relative position between the microscope and the OmSR can be optimised using the LM algorithm based on (22). The position coordinates of the ToSF calculated by (3) in the Cartesian space should also be optimised through the LM algorithm for the reason of movement error of OmSR. The derivative of $\boldsymbol{e}$ with respect to $\mathbf{P}$ can be expressed as follows:

$$\frac{\partial \boldsymbol{e}}{\partial \mathbf{P}} = -\begin{bmatrix} \frac{f_x}{z^c} & 0 & -\frac{f_x x^c}{z^{c2}} \\ 0 & \frac{f_y}{z^c} & -\frac{f_y y^c}{z^{c2}} \end{bmatrix} \boldsymbol{R} \tag{23}$$

For the OmSR system, a commercially available 3-axis Cartesian stage (X-LSQ150B, Zaber Technologies Inc., BC, Canada) is utilised to position the Remote Centre of Motion (RCM) point ($\mathbf{O}$) to coincide with the insertion point on the sclera during the preoperative stage and point ($\mathbf{O}$) is fixed during the intraoperative stage as the 5-DOFs of the OmSR are used to perform the necessary surgical tasks. As a result, the extrinsic matrix $\exp(\xi^\wedge)$ obtained preoperatively remains applicable during the intraoperative stage.

E. Movement Error Compensation Based on Image Depth

To obtain the Cartesian coordinate of the ToSF through image measurement, the following steps are taken: 1) assuming no error in the movement of the ToSF, the distance h between the ToSF and the microscope in Cartesian space can be directly calculated according to relative position $\exp(\xi^\wedge)$ and the known forward kinematic relation (3) in real time; 2) the ToSF is tracked in using the CSR-DCF method to obtain the pixel coordinates $\boldsymbol{u} = [u, v]$, and 3) the Cartesian coordinates of the ToSF are calculated by substituting both the distance h (depth information) and the pixel coordinates $[u, v]$ into (20).

However, the actual movement of the ToSF installed on the OmSR is not completely free of errors, and these potential errors result in a deviation Δ_h in the estimated distance h, leading to inaccurate measurements of the Cartesian coordinates of the ToSF. Based on this, the measurement error associated with Δ_h in the microscope image results in a motion error of the ToSF. On the imaging side, the pixel resolution of the microscope in posterior segment ophthalmic surgery is typically within the clinical acceptable range of $2.4\,\mu\text{m} - 3.3\,\mu\text{m}$. As such it can be ignored, thus the deviation is solely to be attributed to the motion error. By comparing the position of the ToSF estimated based on the microscope images with the desired position $\mathbf{P}_d$ that is used as input into the OmSR admittance control, it can be determined if the ToSF has arrived at the desired position in Cartesian space. If not, the ToSF is controlled to move in the direction of decreasing $\mathbf{P}_{\Delta_h}$ towards $[0, 0, 0]^T$. The motion error of the OmSR can be represented as follows:

$$\mathbf{P}_{\Delta_h} = \Delta_h \cdot \exp(\xi^\wedge)^{-1} \boldsymbol{K}^{-1} \boldsymbol{u} \tag{24}$$

This is because the updated value of the change in focal length f can be obtained from the microscope in real-time and communicated to the OmSR to update the controller accordingly. Thus, the proposed method can be seamlessly applied to the entirety of the surgical procedure, even in the cases when the focal length of the microscope is adjusted intra-operatively.

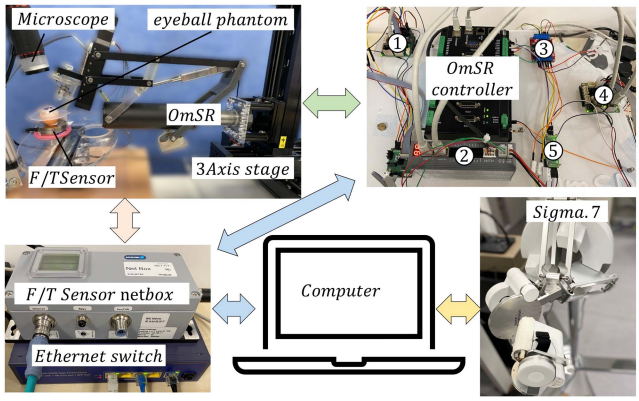

Fig. 4. Setup of the OmSR system. ①②③④⑤ are the controllers of each joint motor.

III. Experimental Validation & Results

A. System Configuration and Setup

As shown in Fig. 4, the complete robot system comprises the OmSR robot, a commercial 3-Axis Cartesian stage, the OmSR controller, the joint motor controllers, a microscope, a commercial F/T sensor, a computer and a Force Dimension Sigma.7 haptic interface (Nyon, Switzerland) used as master device for teleoperation of the system by clinical users. In the experiments, the eyeball phantom (VR eye PS-010, Phillips Studio, Bristol, U.K.) for clinical training is used. This phantom accurately mimics the intricate details of the tissue of the eyeball, including pathologies of the posterior segment. The OmSR controller and the drive motor controllers of each joint communicate using EtherCAT and RS485 protocols, as indicated by the green arrow, and the communication frequency is kept at a minimum of 1 kHz. The F/T sensor connects to the F/T Sensor Netbox through the CAN Bus communication protocol, as shown by the orange arrow. The Ethernet switch device facilitates direct communication between the OmSR controller and F/T Sensor Netbox and the computer through Ethernet, as indicated by the blue arrow. During the teleoperated control stage, the haptic interface Sigma.7 is connected to the computer via USB interface at a frequency of approximately 3 kHz, as indicated by the yellow arrow. The highly precise (50 μm) 3-Axis Cartesian stage can be manually controlled using a knob or automatically through an RS232 communication protocol to ensure the RCM point of the OmSR coincides with the insertion point on the sclera, thus preventing damage. The control programs for the entire robot system in the experiments described in this letter were

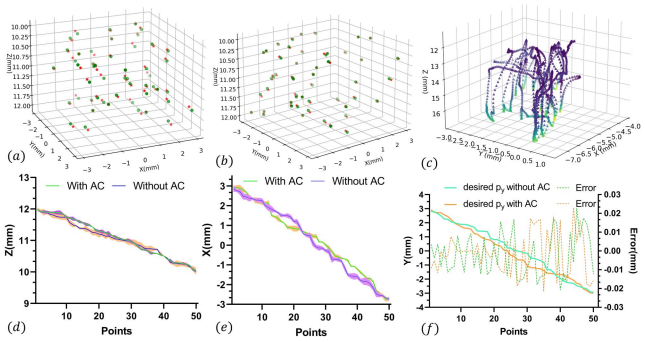

Fig. 5. Figures (a) and (b) shows the results of the application of open-loop control and admittance control, respectively. The motion errors of the ToSF in the X, Y, Z directions under the admittance control ("With AC") and the open-loop control ("Without AC") are depicted in figures (d)–(f) using error bars and polylines. The trajectory of the ToSF in Sec.III-C is presented in figure (c), where the yellow-green curve represents the proximity of the contact force between ToSF and the fundus tissue to the defined threshold, with a lighter colour indicating closer proximity.

implemented using Python 3.9 in Windows 11 $\times$ 64 operating system.

B. Evaluation of Movement Error Compensation Based on Image Measurement

In order to evaluate the accuracy of the position control loop when the admittance controller is active as well as the performance of the motion error compensation, 50 points in the volume defined by $\{p_x \in [-3,3], p_y \in [-3,3], p_z \in [10,12]\}$ inside the eyeball and in the field of view of the microscope were randomly selected and the ToSF was controlled to reach them. The $\exp(\xi^{\wedge})$ was calculated and optimised using the methods outlined in Section II-D. To minimise matching errors, the ToSF was moved to twenty non-coplanar points to obtain $\exp(\xi^{\wedge})$, as depicted in Fig. 3(a). The resulting computation produced both the rotation matrix $\boldsymbol{R}$ and translation matrix t of the microscope relative to the OmSR.

$$\boldsymbol{R} = \begin{bmatrix} 0.265 & 0.4668 & -0.8436 \\ -0.1549 & 0.884 & 0.4406 \\ 0.952 & 0.0138 & 0.3068 \end{bmatrix}, t = \begin{bmatrix} 7.986 \\ -6.1209 \\ 6.791 \end{bmatrix} \quad (25)$$

During motion, the ToSF was not in contact with the fundus tissue, with no interaction forces occurring. The position of ToSF was tracked and its pixel coordinates were calculated using the CSR-DCF method. These pixel coordinates were then substituted into (15) to obtain the Cartesian coordinates of the ToSF. The motion error of ToSF was computed by comparing the measured position coordinates with the desired position coordinates. To provide a comparison and assess the performance of the proposed admittance controller, the ToSF was moved through 50 points using both the open-loop and the admittance controller. The distribution of these points in Cartesian space is shown in Fig. 5(a) and (b), respectively. The green dots represent the desired positions of ToSF, and the red $*$ points represent the positions measured by the microscope. As seen in Fig. 5(b), the red $*$ points are closer to the green dots in Cartesian space, indicating that the motion error of ToSF is significantly smaller with the proposed admittance controller.

To facilitate the analysis of the motion error of ToSF along the three axes (X, Y, Z) of the OmSR coordinate system, the desired coordinate values of the 50 random points were ordered from large to small. The trend curve of the desired coordinates on each axis and the distribution of the motion error bars of the ToSF were then plotted as shown in Fig. 5(d)–(f). The average motion error of the ToSF along the X-axis, Y-axis, and Z-axis using the open-loop controller was 22μm, 2μm, and 14μm, respectively. After compensating for the movement error using the admittance controller based on image feedback, the average error of ToSF along the X-axis, Y-axis, and Z-axis was reduced to $8\,\mu$m, $1.1\,\mu$m, and $8\,\mu$m, respectively. This represents an increase in motion accuracy of 64%, 4.21%, and 43% respectively, thus ensuring that the clinical requirements of posterior surgical procedures in terms of position accuracy of the ToSF are met.

C. Evaluation of Compliance Control Method

To evaluate the efficacy of the proposed compliance control in membrane peeling and in general needle insertion application, e.g. retinal blood vessel cannulation, the test rig shown in Fig. 4 was used. The output signal of the F/T sensor was filtered using a 73 Hz low-pass filter to reduce the impact of high-frequency noise on the force measurement. The F/T sensor was tared by computing the average of the first 100 measurement data read. In the set of experiments presented the ToSF was controlled by a specialist clinician with no specific training on the OmSR system. The system was teleoperated using the haptic interface Sigma.7 with the goal of peeling off the membrane and inserting the needle into fundus tissue. The trajectory of the ToSF in Cartesian space was obtained in Fig. 5(c). In the compliance control framework, the desired force and threshold force was set to 40 mN and 60 mN according to the tool-tissue force thresholds proposed in [4] for posterior segment surgical procedures. The experimental results of the application of the compliance control to the OmSR are displayed in Fig. 6. The mean, mode, median and STD of forces are 25.9 mN, 11.58 mN, 14.2 mN and 24.6 mN respectively. Here, the contact forces are collected in the ILM peeling procedure. A comparison between the desired trajectory input from Sigma.7 and the real trajectory followed by the OmSR reveals good consistency both in terms of time and position of the ToSF in the Cartesian space. In the procedure the ToSF makes contact with the tissue without exceeding the threshold; the maximum dynamic adjustment distance of the ToSF is controlled by the admittance controller, and it can reach $35.2\,\mu\text{m} \pm$ motion error. This ensures that the tissue is well protected from potential damage caused by the stiffness of OmSR.

These results demonstrate that the proposed compliance controller can effectively adjust the position of the ToSF towards the desired position in real-time ensuring the threshold for the interaction force is not exceeded, thereby safeguarding the tissue from potential harm. If the contact force exceeds the preset threshold, the Sigma.7 haptic controller provides a reaction force of approximately 1.5 N to the hands of the surgeon to

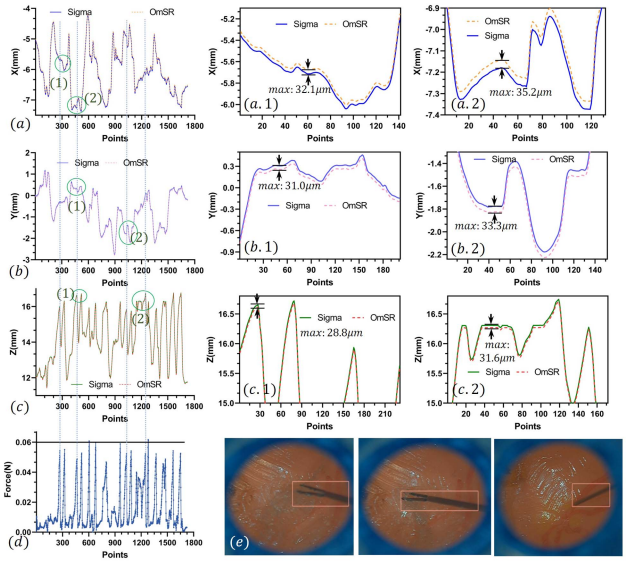

Fig. 6. Figures (a)–(c) show the projections of the trajectory of ToSF along the X-axis, Y-axis, and Z-axis of the OmSR coordinate system, respectively. The label $Points$ on the horizontal axis represents the number of collected data on the position of ToSF, and thus the duration of the movement. Figures (a.1) and (a.2) provide a magnified view of the curve inside the number (1) and (2) green ellipses in figure (a). The same naming conventions are used for figures (b.1), (b.2), (c.1), and (c.2). Figure (d) depicts the changes in contact force. In figure (e) ILM peeling and needle insertion procedures are presented.

alert them of the threshold being reached. The movement of the hand of the surgeon is thereby prevented from continuing in a direction that would increase the force. Additionally, the control system disconnects the command signal from Sigma.7 to OmSR, ensuring that the OmSR continues to move in a direction that reduces the increasing force. This double-layered approach ensures patient safety during the procedure.

IV. Conclusion

In this study, we proposed a vision-and-force-based compliance control method for a posterior segment ophthalmic surgical robot. This method allows for precise motion control of the ToSF by incorporating contact force measurements between the ToSF and the fundus tissue, thereby ensuring accuracy while avoiding damage to the targeted tissue. Motion accuracy is improved through visual feedback from a microscope to measure the position of the ToSF in Cartesian space and feedback of the motion error to the position control loop of the admittance controller. The challenges associated with the inaccuracies occurring in the evaluation of the relative position between the microscope and the OmSR are solved at software level through the EPnP, feature matching and error optimisation methods. The experimental results showed that the proposed compliance control method limits the maximum motion error of the EE of the system to 8μm, representing a substantial improvement of up to 64% compared to the open-loop control proposed in our previous work. The compliance control can effectively adjust the position of the ToSF while having good consistency both in terms of time and space when contact force exists between forceps and tissue.

References

[1] W. H. Organization, "World report on vision," 2019. [Online]. Available: https://www.who.int/publications/i/item/9789241516570
[2] D. Silver and A. Csutak, "Human eye dimensions for pressure-volume relations," *Invest. Ophthalmol. Vis. Sci.*, vol. 51, no. 13, p. 5019, 2010.
[3] C. Riviere, R. S. Rader, and P. Khosla, "Characteristics of hand motion of eye surgeons," in *Proc. 19th Annu. Int. Conf. IEEE Eng. Med. Biol. Soc.*, 1997, pp. 1690–1693.
[4] A. K. G. Miss, G. Mylonas, and H. Marcus, "Tool-tissue forces in surgery: A systematic review," *J. Amer. College Surgeons*, vol. 233, no. 5, 2021, Art. no. e70.
[5] C. Haritoglou, C. A. Gass, M. Schaumberger, A. Gandorfer, M. W. Ulbig, and A. Kampik, "Long-term follow-up after macular hole surgery with internal limiting membrane peeling," *Amer. J. Ophthalmol.*, vol. 134, no. 5, pp. 661–666, 2002.
[6] J. Xiao, Q. Wu, D. Sun, C. He, and Y. Chen, "Classifications and functions of vitreoretinal surgery assisted robots-a review of the state of the art," in *Proc. IEEE Int. Conf. Intell. Transp., Big Data Smart City*, 2019, pp. 474–484.
[7] B. Gonenc, A. Chamani, J. Handa, P. Gehlbach, R. H. Taylor, and I. Iordachita, "3-DoF force-sensing motorized micro-forceps for robot-assisted vitreoretinal surgery," *IEEE Sensors J.*, vol. 17, no. 11, pp. 3526–3541, Jun. 2017.
[8] T. Edwards et al., "First-in-human study of the safety and viability of intraocular robotic surgery," *Nature Biomed. Eng.*, vol. 2, no. 9, pp. 649–656, 2018.
[9] M. Draelos, G. Tang, B. Keller, A. Kuo, K. Hauser, and J. A. Izatt, "Optical coherence tomography guided robotic needle insertion for deep anterior lamellar keratoplasty," *IEEE Trans. Biomed. Eng.*, vol. 67, no. 7, pp. 2073–2083, Jul. 2020.
[10] Y. Koyama, M. M. Marinho, M. Mitsuishi, and K. Harada, "Autonomous coordinated control of the light guide for positioning in vitreoretinal surgery," *IEEE Trans. Med. Robot. Bionics*, vol. 4, no. 1, pp. 156–171, Feb. 2022.
[11] H. Li et al., "An admittance-controlled amplified force tracking scheme for collaborative lumbar puncture surgical robot system," *Int. J. Med. Robot. Comput. Assist. Surg.*, vol. 18, no. 5, 2022, Art. no. e2428.
[12] K. Mach et al., "OCT-guided robotic subretinal needle injections: A deep learning-based registration approach," in *Proc. IEEE Int. Conf. Bioinf. Biomed.*, 2022, pp. 781–786.
[13] C. He et al., "Toward safe retinal microsurgery: Development and evaluation of an RNN-based active interventional control framework," *IEEE Trans. Biomed. Eng.*, vol. 67, no. 4, pp. 966–977, Apr. 2020.
[14] C. Ott, R. Mukherjee, and Y. Nakamura, "Unified impedance and admittance control," in *Proc. IEEE Int. Conf. Robot. Automat.*, 2010, pp. 554–561.
[15] N. Wang, X. Zhang, M. Li, H. Zhang, D. Stoyanov, and A. Stilli, "A 5-DOFs robot for posterior segment eye microsurgery," *IEEE Robot. Automat. Lett.*, vol. 7, no. 4, pp. 10128–10135, Oct. 2022.
[16] M. Li, X. Zhang, N. Wang, H. Zhang, and X. Feng, "Structure design and dimension optimization of FBG enhanced sensitization equipment for measuring axial tactile micro-force of macular hole ophthalmic surgical robot," in *Proc. WRC Symp. Adv. Robot. Automat.*, 2022, pp. 179–184.
[17] X. He, M. Balicki, P. Gehlbach, J. Handa, R. Taylor, and I. Iordachita, "A multi-function force sensing instrument for variable admittance robot control in retinal microsurgery," in *Proc. IEEE Int. Conf. Robot. Automat.*, 2014, pp. 1411–1418.
[18] Leica Microsystems, "Proveo 8 surgical microscope," 2023. [Online]. Available: https://www.leica-microsystems.com/products/surgical-microscopes/p/proveo-8/
[19] N. Jacobson, *Lie Algebras*. Mineola, NY, USA: Dover Publication, 1979.
[20] V. Lepetit, F. Moreno-Noguer, and P. Fua, "EP*n*P: An accurate O(n) solution to the P*n*P problem," *Int. J. Comput. Vis.*, vol. 81, pp. 155–166, 2009.
[21] T. Lindeberg, "Scale invariant feature transform," vol. 7, no. 5, p. 10491, 2012.
[22] A. Lukezic, T. Vojir, L. Čehovin Zajc, J. Matas, and M. Kristan, "Discriminative correlation filter with channel and spatial reliability," in *Proc. IEEE Conf. Comput. Vis. Pattern Recognit.*, 2017, pp. 6309–6318.
[23] G. Xiang, Z. Tao, L. Yi, and Y. Qinrui, *Visual SLAM Lecture Fourteen: From Theory to Practice*. Electronic Industry Press, 2017.
[24] A. Ranganathan, "The Levenberg-Marquardt algorithm," *Tutoral LM Algorithm*, vol. 11, no. 1, pp. 101–110, 2004.
[25] K. Bull, J.-Y. Desaules, and Z. Papić, "Quantum scars as embeddings of weakly broken Lie algebra representations," *Phys. Rev. B*, vol. 101, no. 16, 2020, Art. no. 165139.